Table S1. Targets information for molecular docking.

Gene Name	Uniprot ID	Protein Name	3D structure ID
AKT1	P31749	AKT1_HUMAN	AF-P31749-F1
HIF1A	Q16665	HIF1A_HUMAN	AF-Q16665-F1
MAPK1	P28482	MK01_HUMAN	AF-P28482-F1
MAPK3	P27361	MK03_HUMAN	AF-P27361-F1
MTOR	P42345	MTOR_HUMAN	AF-P42345-F1
PIK3CA	P42336	PK3CA_HUMAN	AF-P42336-F1
RELA	Q04206	TF65_HUMAN	AF-Q04206-F1

Table S2. Primer sequences for RT-qPCR (mouse).

ID	Primer
HIF-1α(mouse)	Forward：5’- CTTGACAAGCTAGCCGGAGG-3’
	Reverse：5’- AAGAGACAAGTCCAGAGGCG-3’
HK2(mouse)	Forward：5’-CTGCTTTGGAGATCCGAGGG-3’
	Reverse：5’-GTCTAGCTGCTTAGCGTCCC-3’
PKM2(mouse)	Forward：5’-GCTCTAGGTATCGCAGCAGG-3’
	Reverse：5’-AGTCCCTGCTTCACTGTGTG-3’
β-actin(mouse)	Reverse：5’-TGAGCTGCGTTTTACACCCT-3’
	Reverse：5’-GCCTTCACCGTTCCAGTTTT-3’

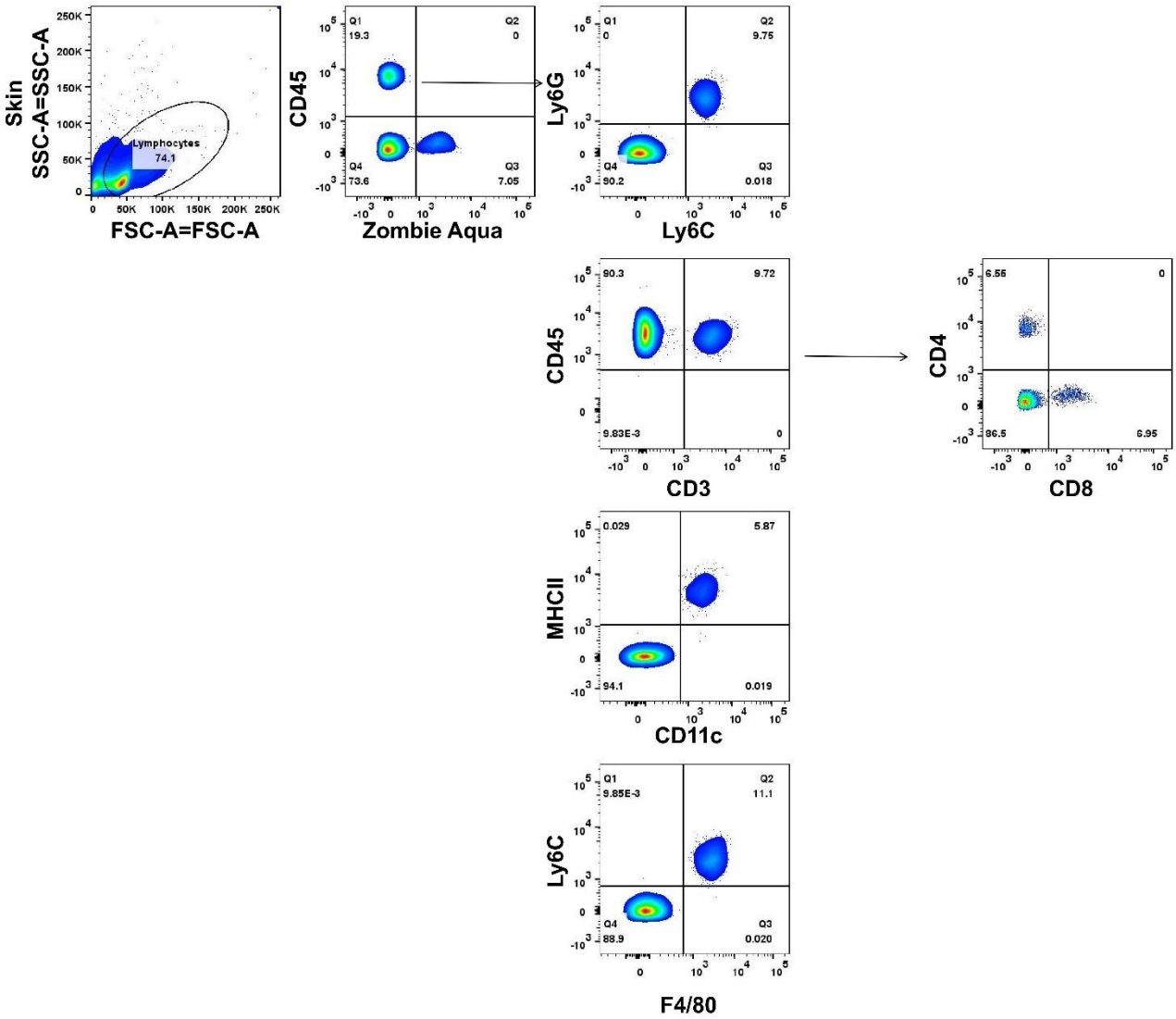

Figure S1. Gating strategy for neutrophil isolation from skin tissue and identification of immune cell subsets.

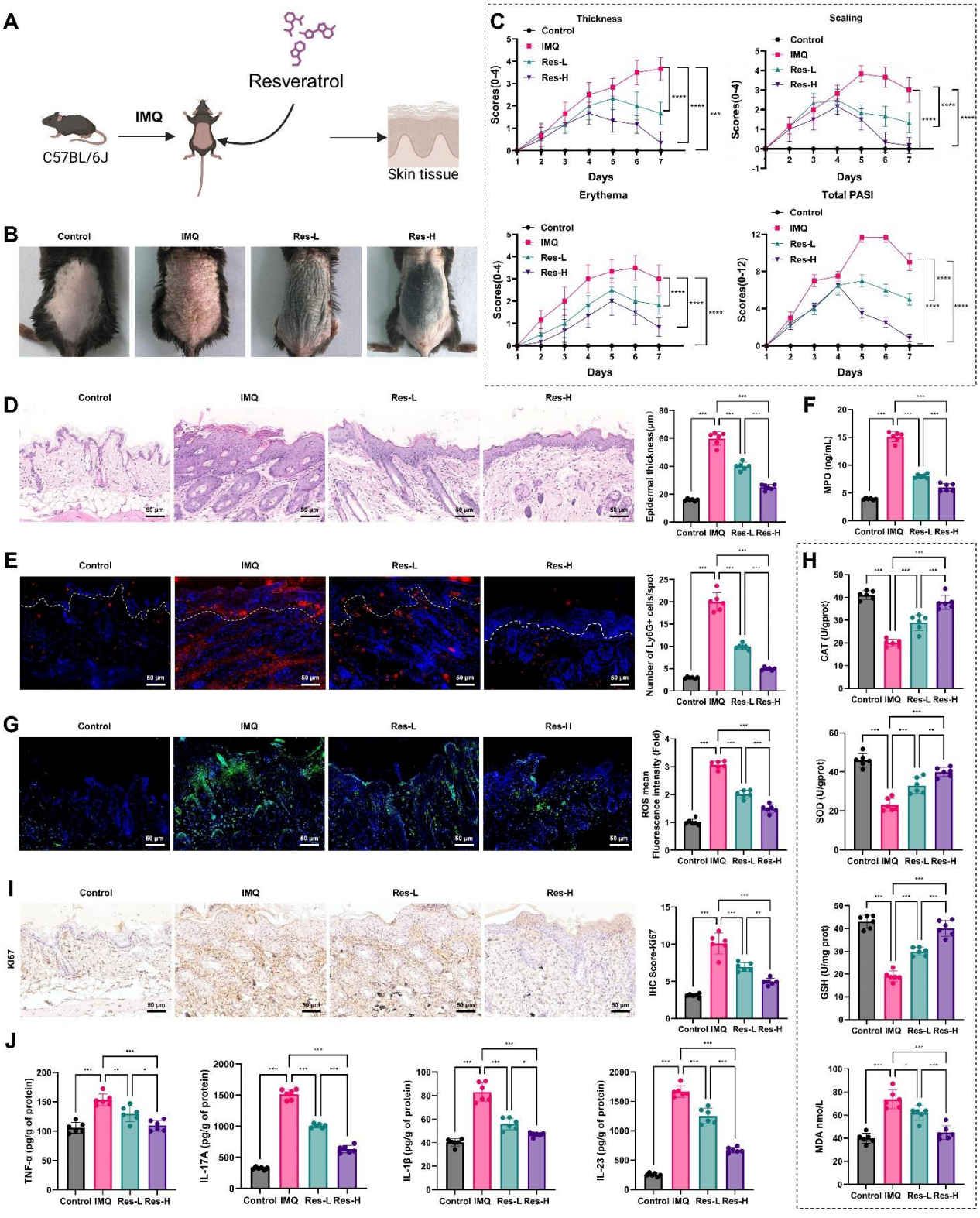

Figure S2. Effects of Res on IMQ-induced psoriasiform skin inflammation.

Note: (A) Schematic diagram illustrating the experimental design of IMQ-induced psoriasiform skin inflammation and Res intervention; (B) Representative images of dorsal skin in IMQ-induced mice, showing scaling, erythema, and inflammatory infiltration; (C) Clinical scores of dorsal skin

over 7 consecutive days after IMQ treatment, including skin thickness, scaling, erythema, and total PASI score; (D) H&E staining of skin tissue to evaluate pathological changes and quantify epidermal thickness; (E) IF co-localization of Ly6G and DAPI to assess neutrophil infiltration, bar: 50 μm; (F) Colorimetric assay to determine MPO activity in mouse skin tissues; (G) DCFH-DA staining to detect ROS levels in skin tissues, bar: 50 μm; (H) Colorimetric analysis of MDA content and activities of SOD, GSH, and CAT in skin tissues; (I) IHC staining to assess expression of the proliferation marker Ki67 in skin, bar: 50 μm; (J) ELISA detection of IL-23, IL-1β, IL-17A, and TNF-α secretion levels in lesional skin tissues. Each group included six animals. *$p < 0.05$, **$p < 0.01$, ***$p < 0.001$.

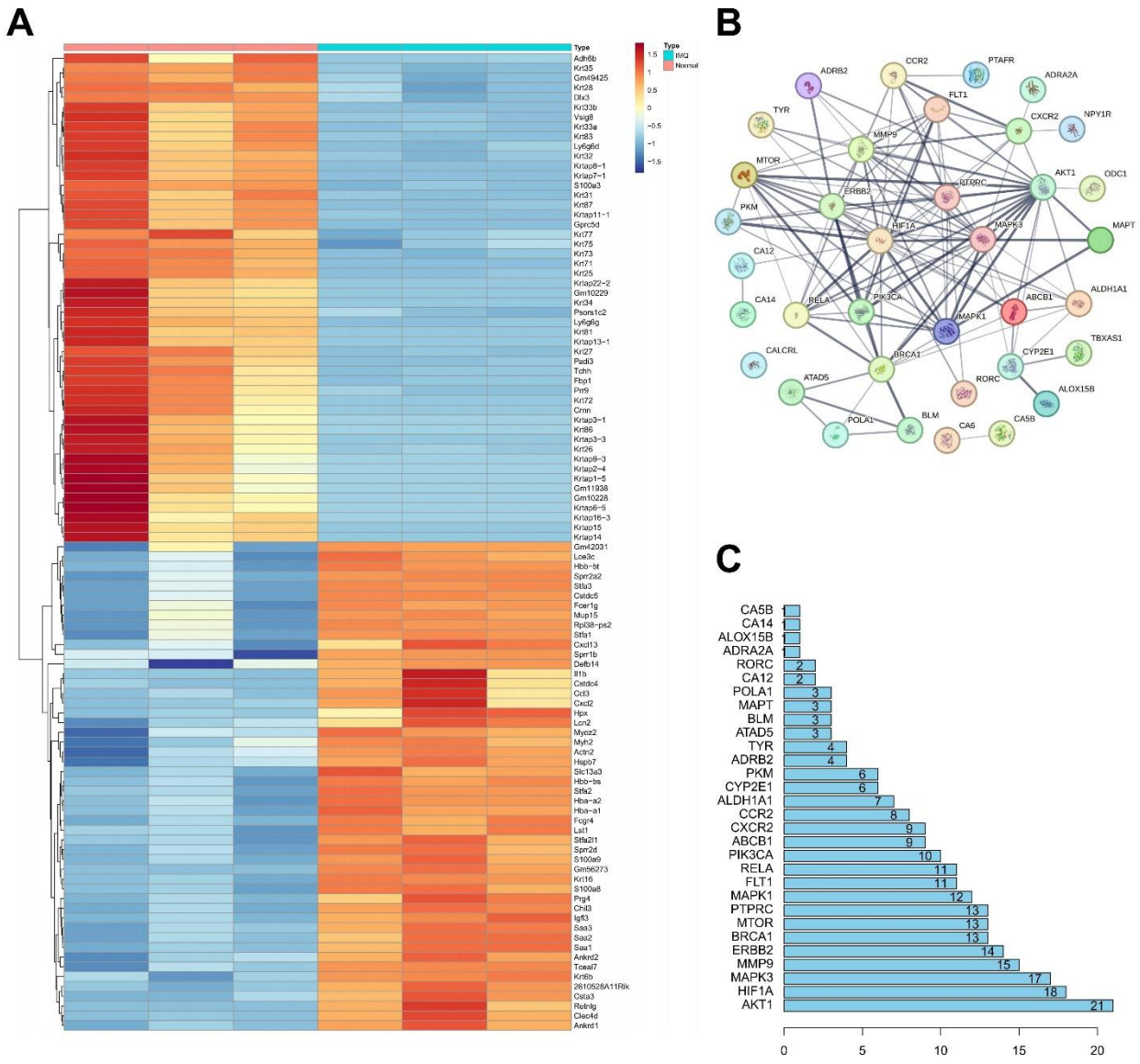

Figure S3. Potential target identification of Res in psoriasis treatment.

Note: (A) Heatmap of DEGs from RNA-seq data comparing the Normal group (n = 3) and IMQ group (n = 3), showing the top 50 upregulated and top 50 downregulated genes ranked by log_2FC; (B) PPI network of the 36 key target genes; (C) Interaction statistics among the 36 target genes.

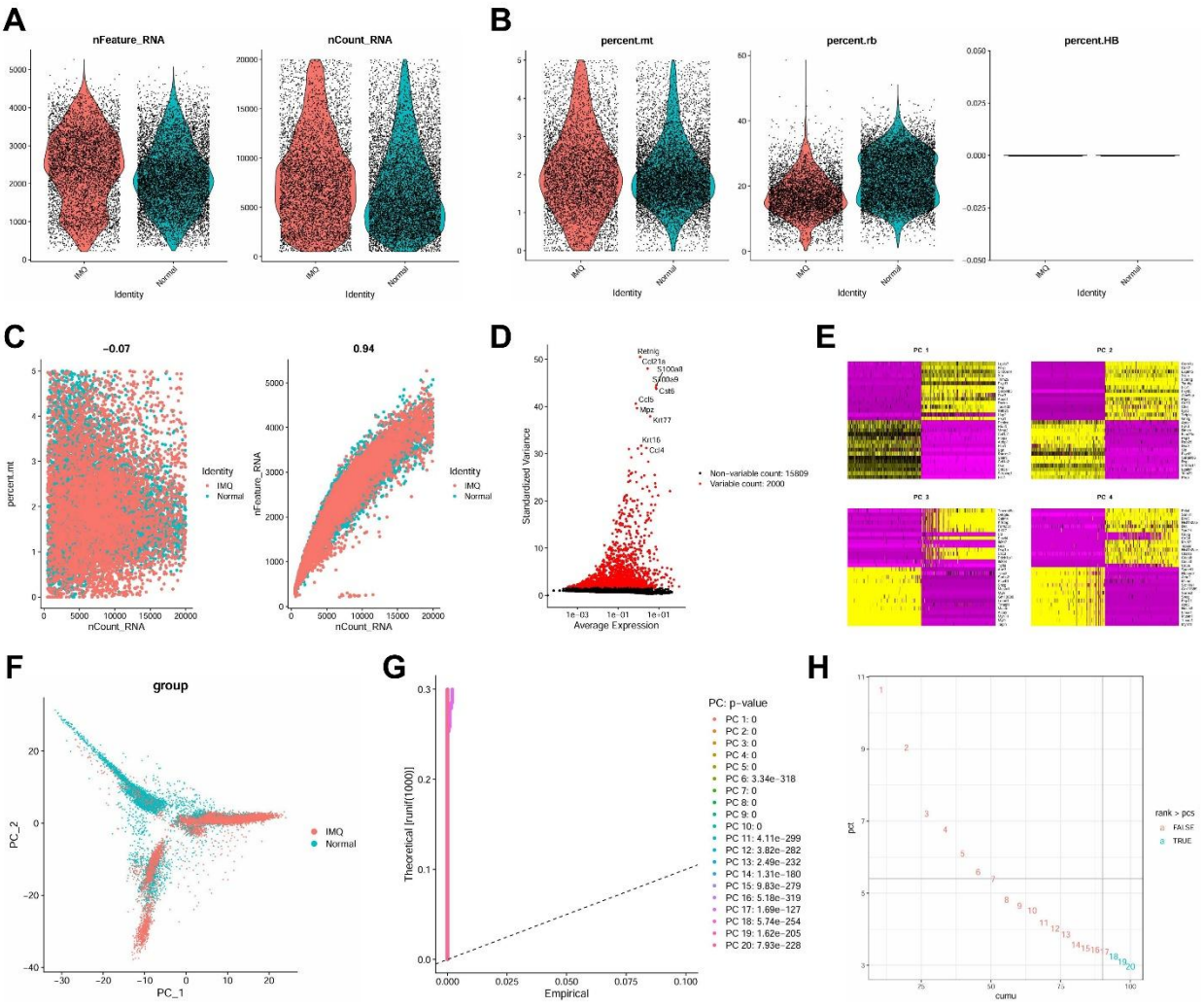

Figure S4. Quality control and dimensionality reduction (PC selection) of filtered scRNA-seq data.

Note: (A) Violin plots of nFeature_RNA and nCount_RNA after data filtering; (B) Violin plots showing percent.mt, percent.rb, and percent.HB distributions; (C) Correlation analysis plots: nCount_RNA vs. percent.mt and nCount_RNA vs. nFeature_RNA; (D) Scatter plot of gene expression variance, with red dots indicating HVGs selected for PCA; (E) Heatmap of the top 30 genes associated with PC_1 to PC_4 in PCA, where yellow indicates upregulation and purple indicates downregulation; (F) Two-dimensional distribution of cells along PC_1 and PC_2; (G) Distribution of *p*-values for PC_1 to PC_20 in PCA compared to the uniform distribution (dashed line), with significant PCs above the line; (H) Elbow plot of SD contribution for each PC, with optimal PCs for downstream analysis highlighted in orange.

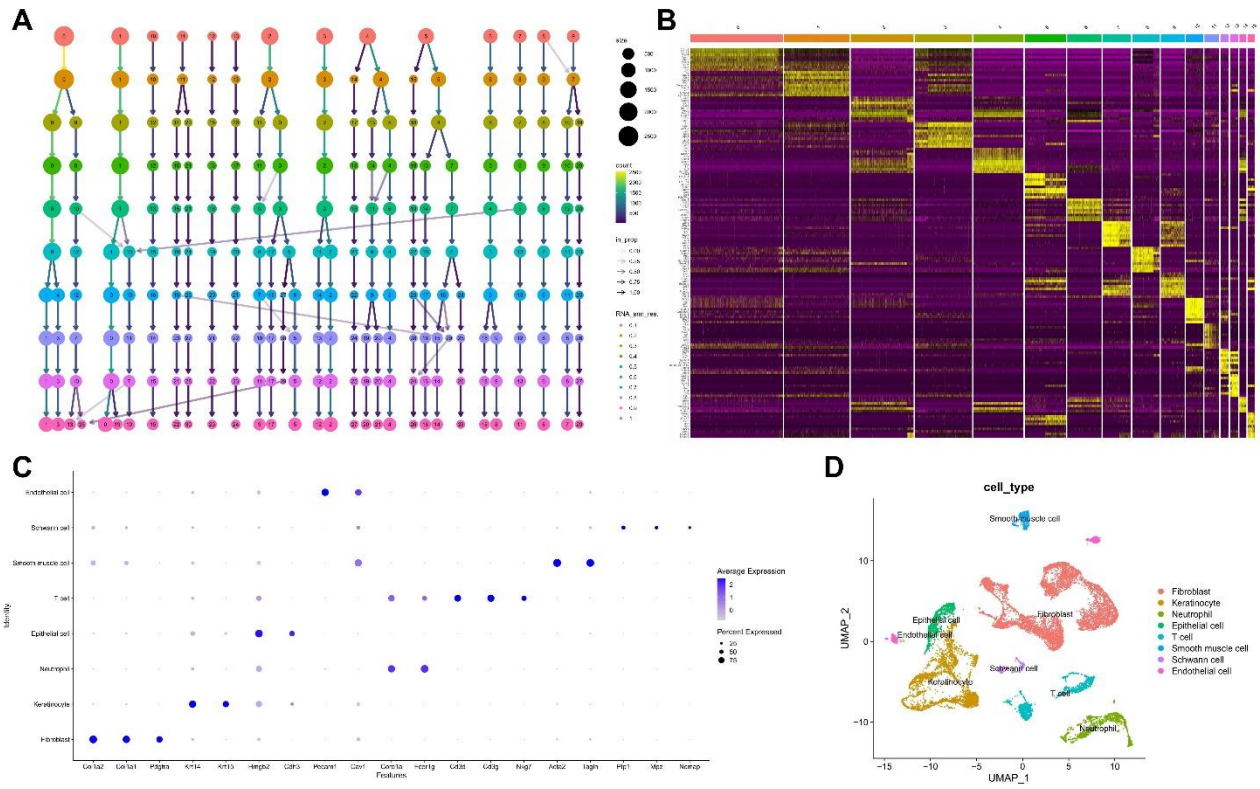

Figure S5. Clustering analysis and marker gene selection for cell type annotation in scRNA-seq data.

Note: (A) Visualization of clustering results under different resolutions (0.1-1); (B) Heatmap of the top 10 marker genes for each cluster, with yellow indicating upregulation and purple indicating downregulation; (C) Dot plot showing expression patterns of selected marker genes used for cell type annotation; (D) UMAP plot of annotated cell types, combining data from both Normal and IMQ groups.

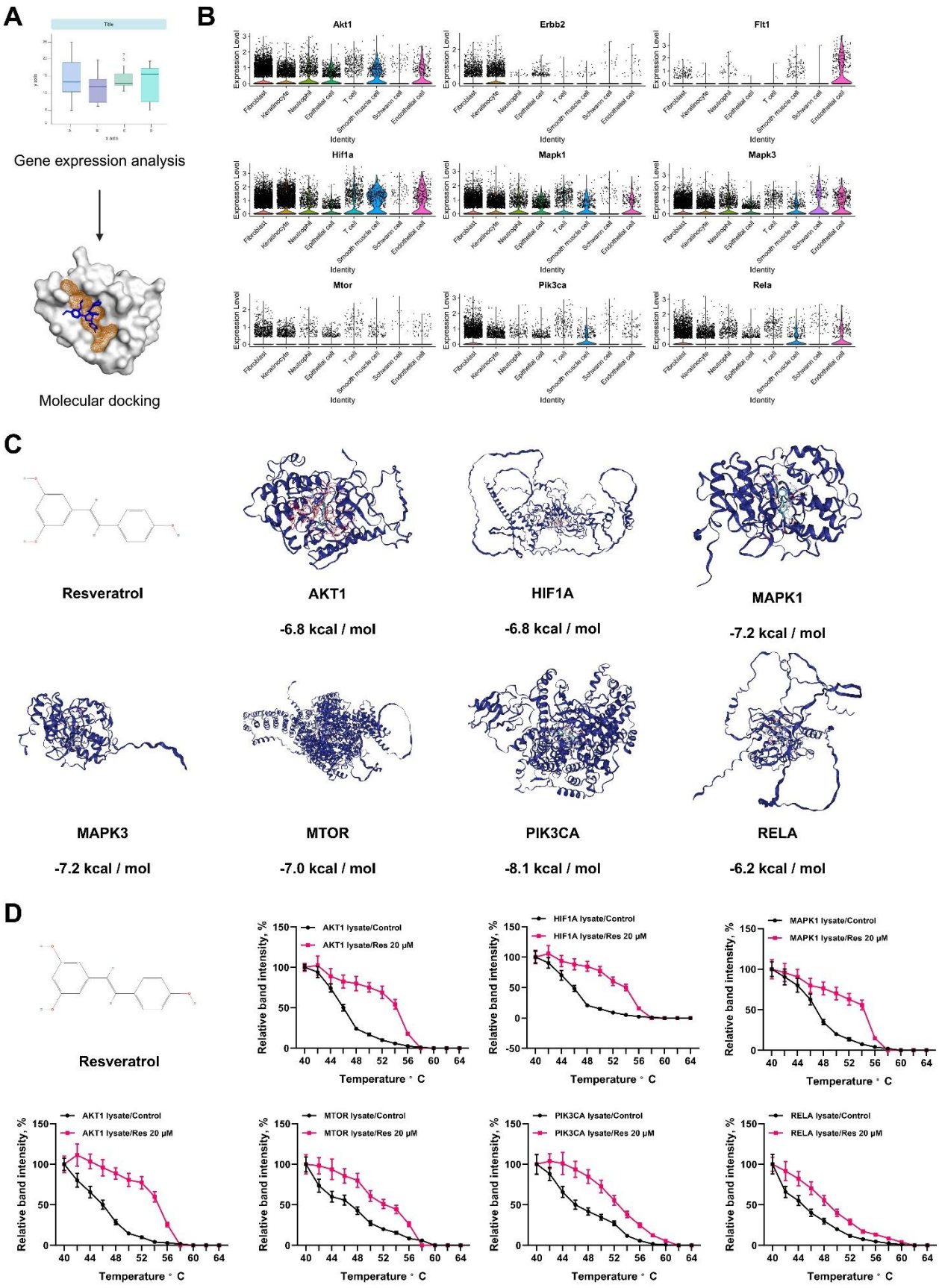

Figure S6. Binding analysis between Res and proteins in the HIF-1 signaling axis.

Note: (A) Flowchart illustrating the analysis of Res binding to proteins in the HIF-1 signaling axis;

(B) Expression of key HIF-1 signaling pathway targets in scRNA-seq data; (C) 2D structure of Res and molecular docking models showing its interactions with AKT1, HIF1A, MAPK1, MAPK3, MTOR, PIK3CA, and RELA, including 3D structures of small molecules and secondary structures of receptor proteins; (D) Protein mobility shift assays demonstrated the binding capability of Res to AKT1, HIF1A, MAPK1, MAPK3, MTOR, PIK3CA, and RELA proteins.

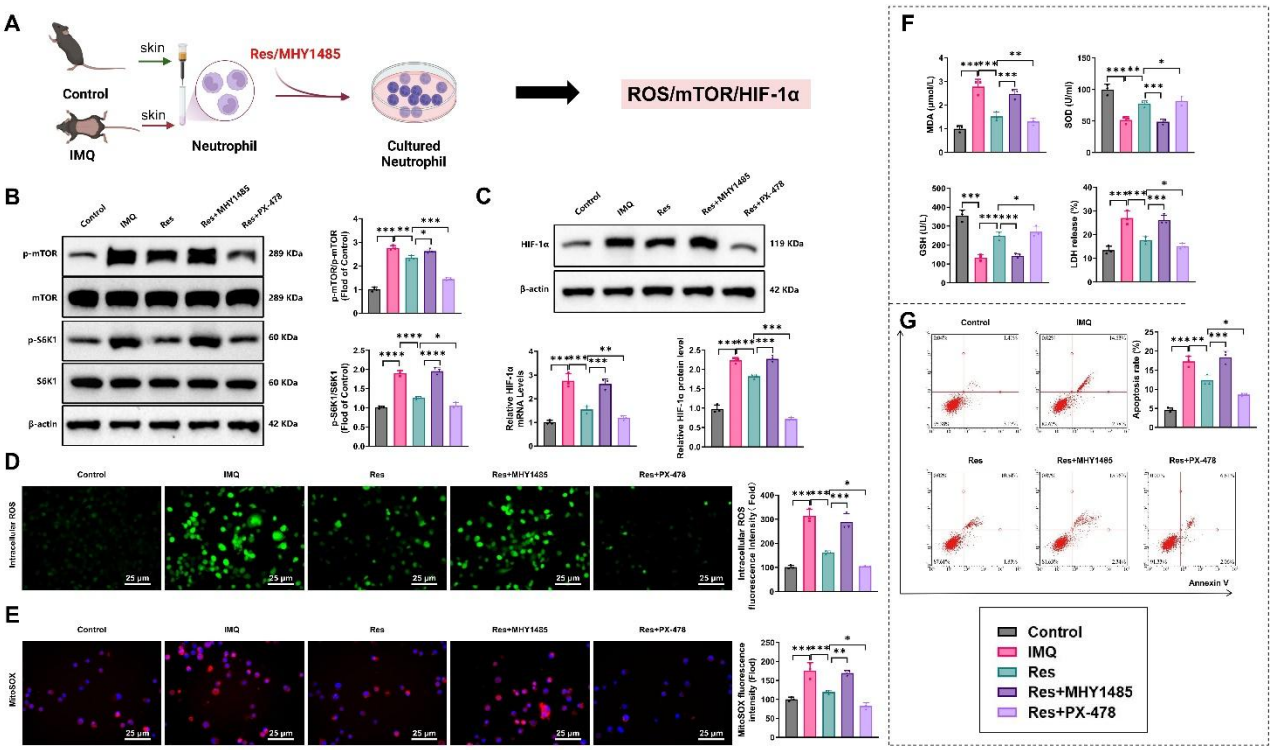

Figure S7. Effects of Res on the ROS/mTOR/HIF-1α axis in IMQ-induced neutrophils.

Note: (A) Flowchart of neutrophil isolation and treatment; (B) Western blot analysis of p-mTOR/mTOR and p-S6K1/S6K1 protein expression in neutrophils; (C) RT-qPCR and Western blot analysis of HIF-1α mRNA and protein expression; (D) DCFH-DA fluorescent probe for detecting intracellular total ROS levels in neutrophils, scale bar = 25 μm; (E) MitoSOX staining for mitochondrial ROS levels in neutrophils, scale bar = 25 μm; (F) MDA, GSH, SOD, and LDH assay kits for oxidative stress markers in neutrophils; (G) Annexin V/PI double staining and flow cytometry analysis of neutrophil apoptosis. Experiments were repeated three times. *$p < 0.05$, **$p < 0.01$, ***$p < 0.001$ between groups.

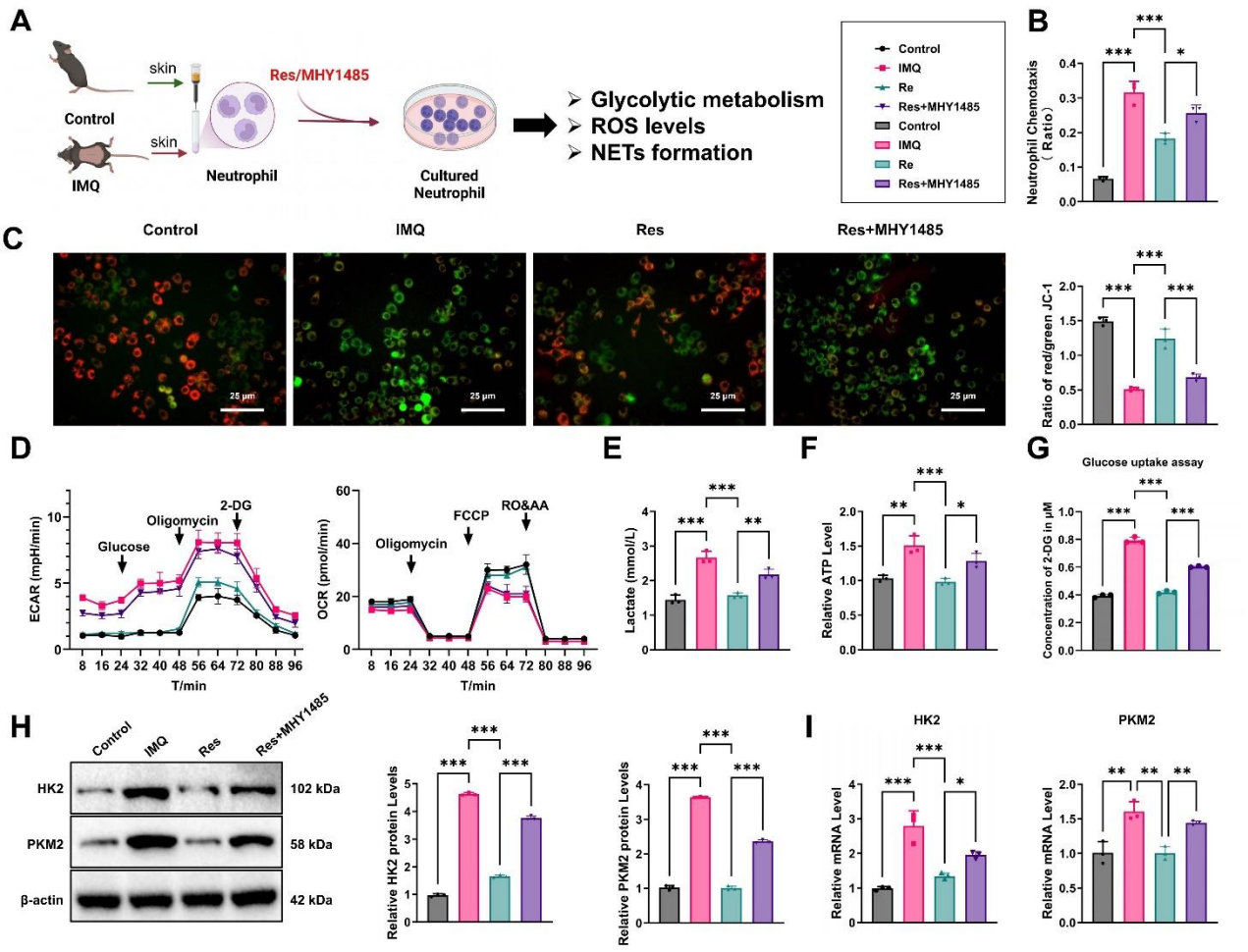

Figure S8. Inhibition of mitochondrial ROS by Res modulates the mTOR/HIF-1α axis and neutrophil metabolic reprogramming.

Note: (A) Flowchart of neutrophil isolation and treatment grouping; (B) fMLP chemotaxis assay for neutrophil chemotactic ability across groups; (C) JC-1 staining for ΔΨm changes in neutrophils, scale bar = 25 μm; (D) Seahorse XF metabolic analysis of OCR and ECAR in neutrophils; (E-G) Detection of lactate production, glucose consumption, and ATP generation to evaluate glycolytic activity in neutrophils; (H-I) RT-qPCR and Western blot analysis of HK2 and PKM2 mRNA and protein expression. Experiments were repeated three times. *$p < 0.05$, **$p < 0.01$, ***$p < 0.001$ between groups.

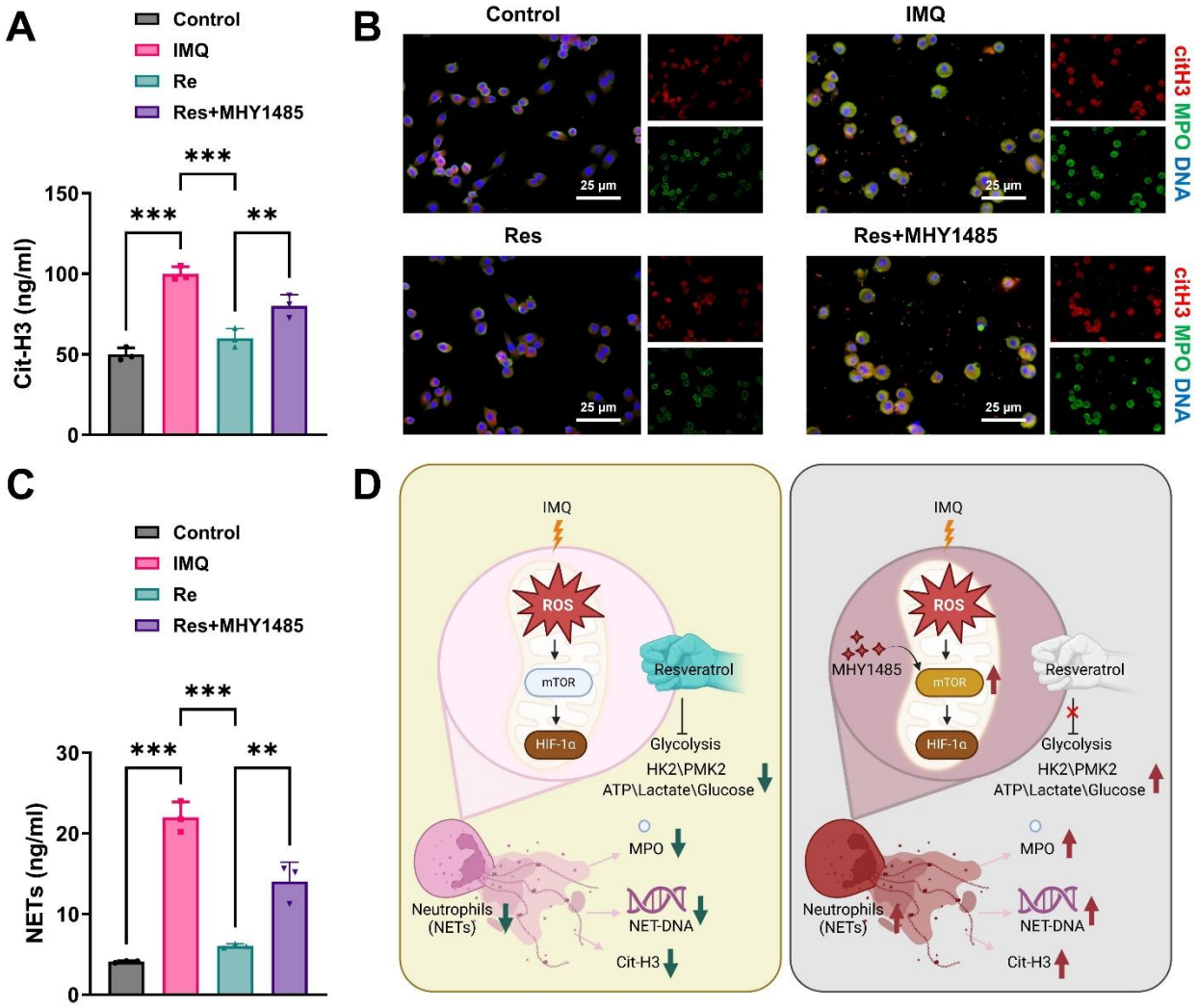

Figure S9. Effects of Res on NETs formation in neutrophils.

Note: (A) ELISA detection of the NETs marker Cit-H3 expression; (B) IF colocalization analysis of MPO (green), Cit-H3 (red), and DNA (blue) in neutrophils, scale bar = 25 μm; (C) PicoGreen probe detection of extracellular DNA release in culture supernatants; (D) Schematic diagram illustrating that Res inhibits NETs formation via suppression of the ROS/mTOR/HIF-1α axis. Experiments were repeated three times. $^{**}p < 0.01$, $^{***}p < 0.001$ between groups.

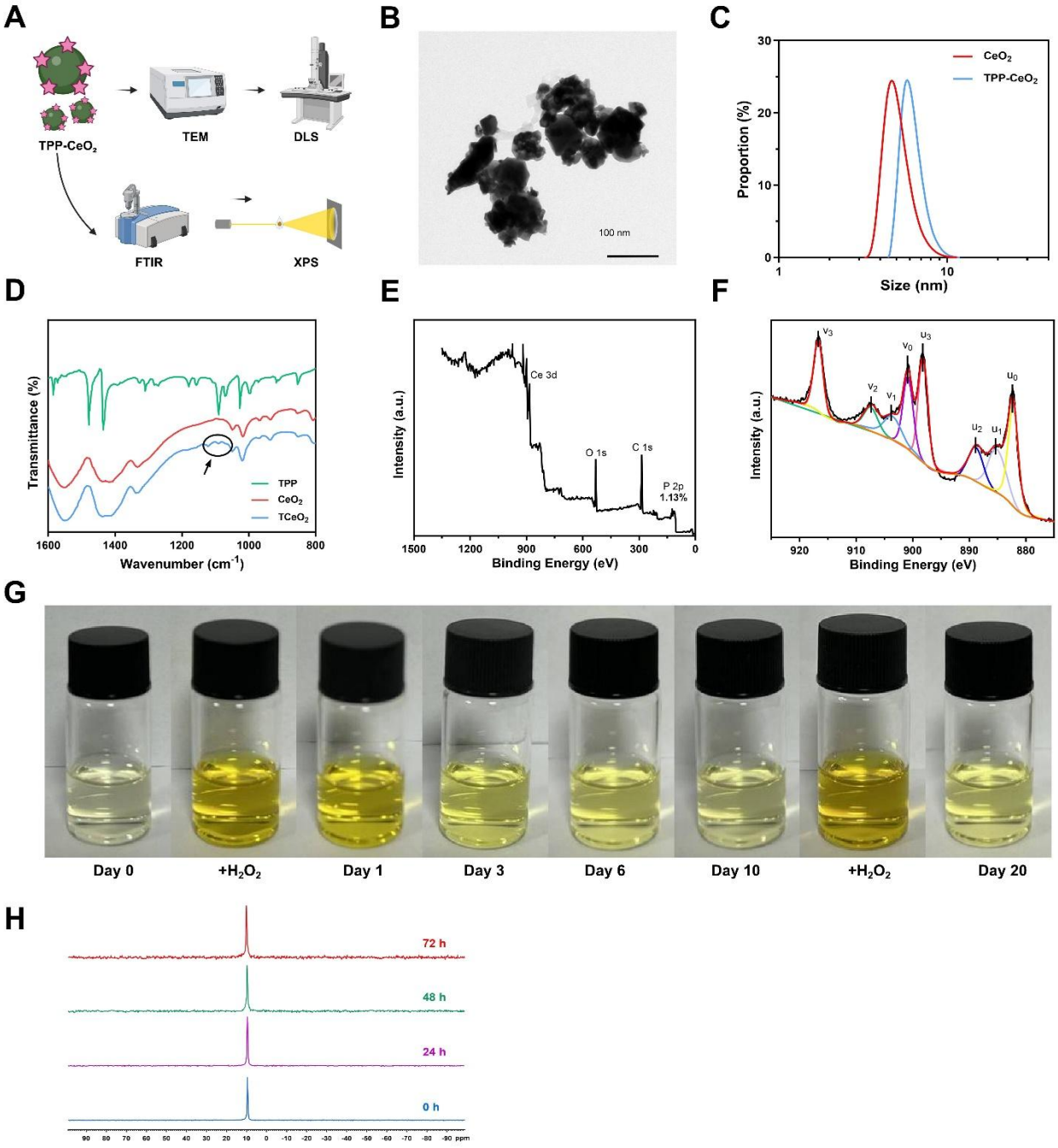

Figure S10. Synthesis and characterization of TPP-CeO_2 nanoparticles.

Note: (A) Schematic illustration of the reverse micelle method for synthesizing TPP-CeO_2 nanoparticles; (B) TEM images showing the morphology and size of CeO_2 and TPP-CeO_2 nanoparticles; (C) DLS analysis of the particle size distribution of CeO_2 and TPP-CeO_2 nanoparticles; (D) FTIR analysis of surface modification on CeO_2 and TPP-CeO_2 nanoparticles; (E) XPS analysis of the phosphorus signal on the surface of TPP-CeO_2 nanoparticles; (F) Ce 3d XPS

spectra showing the coexistence of Ce^{3+} and Ce^{4+} on the surface of TPP-CeO_2 nanoparticles; (G) Color change of the TPP-CeO_2 nanoparticle suspension indicating Ce^{3+}/Ce^{4+} redox conversion capability; (H) NMR analysis was performed to assess the oxidative stability and adsorption characteristics of TPP.

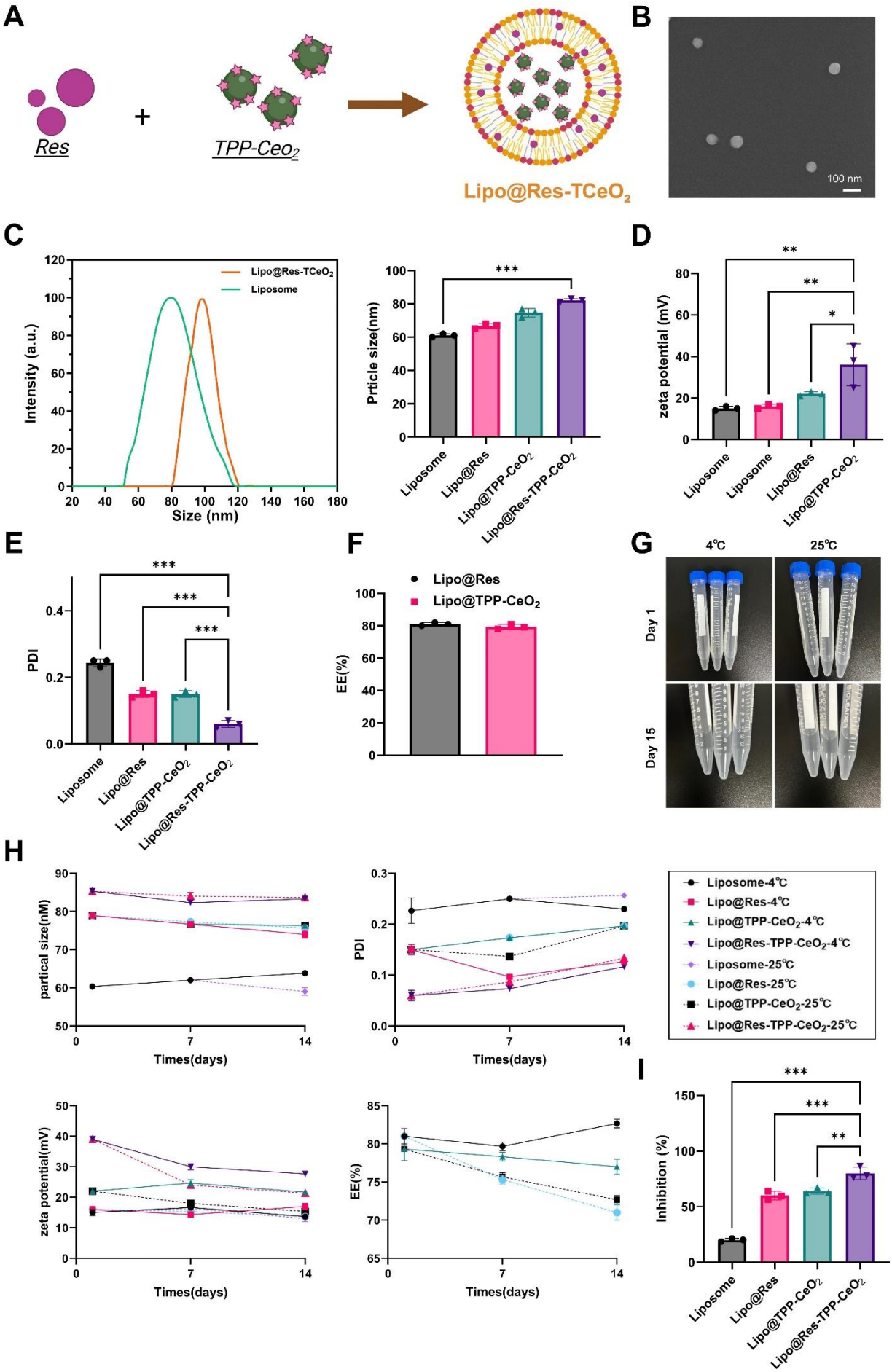
A
Res
TPP-Ceo2
Lipo@Res-TCeO2
B
100 nm
C
Lipo@Res-TCeO2
Liposome
Intensity (a.u.)
Size (nm)
Prticle size(nm)
Liposome
Lipo@Res
Lipo@TPP-CeO2
Lipo@Res-TPP-CeO2
D
zeta potential (mV)
E
PDI
F
Lipo@Res
Lipo@TPP-CeO2
EE(%)
G
4℃
25℃
Day 1
Day 15
H
partical size(nM)
Times(days)
PDI
zeta potential(mV)
EE(%)
Liposome-4℃
Lipo@Res-4℃
Lipo@TPP-CeO2-4℃
Lipo@Res-TPP-CeO2-4℃
Liposome-25℃
Lipo@Res-25℃
Lipo@TPP-CeO2-25℃
Lipo@Res-TPP-CeO2-25℃
I
Inhibition (%)

Figure S11. Preparation and characterization of Lipo@Res-TCeO$_2$.

Note: (A) Schematic diagram of the preparation process for Lipo@Res-TCeO$_2$ liposomes; (B) TEM images of Lipo@Res-TCeO$_2$ liposomes showing morphology and structure, scale bar = 100 nm; (C) DLS analysis of particle size distribution of Lipo@Res-TCeO$_2$ liposomes; (D-E) Zeta potential and PDI analysis indicating surface charge and colloidal stability of Lipo@Res-TCeO$_2$ liposomes; (F) EE of Res and TPP-CeO$_2$ in Lipo@Res-TCeO$_2$ liposomes; (G) Physical stability of Lipo@Res-TCeO$_2$ liposomes after 15 days of storage at 4 °C and 25 °C; (H) Changes in particle size, EE, zeta potential, and PDI after 14 days of storage at 4 °C; (I) Antioxidant capacity of Lipo@Res-TCeO$_2$ liposomes evaluated by DPPH radical scavenging assay. Experiments were repeated three times. *$p < 0.05$, **$p < 0.01$, ***$p < 0.001$ between groups.

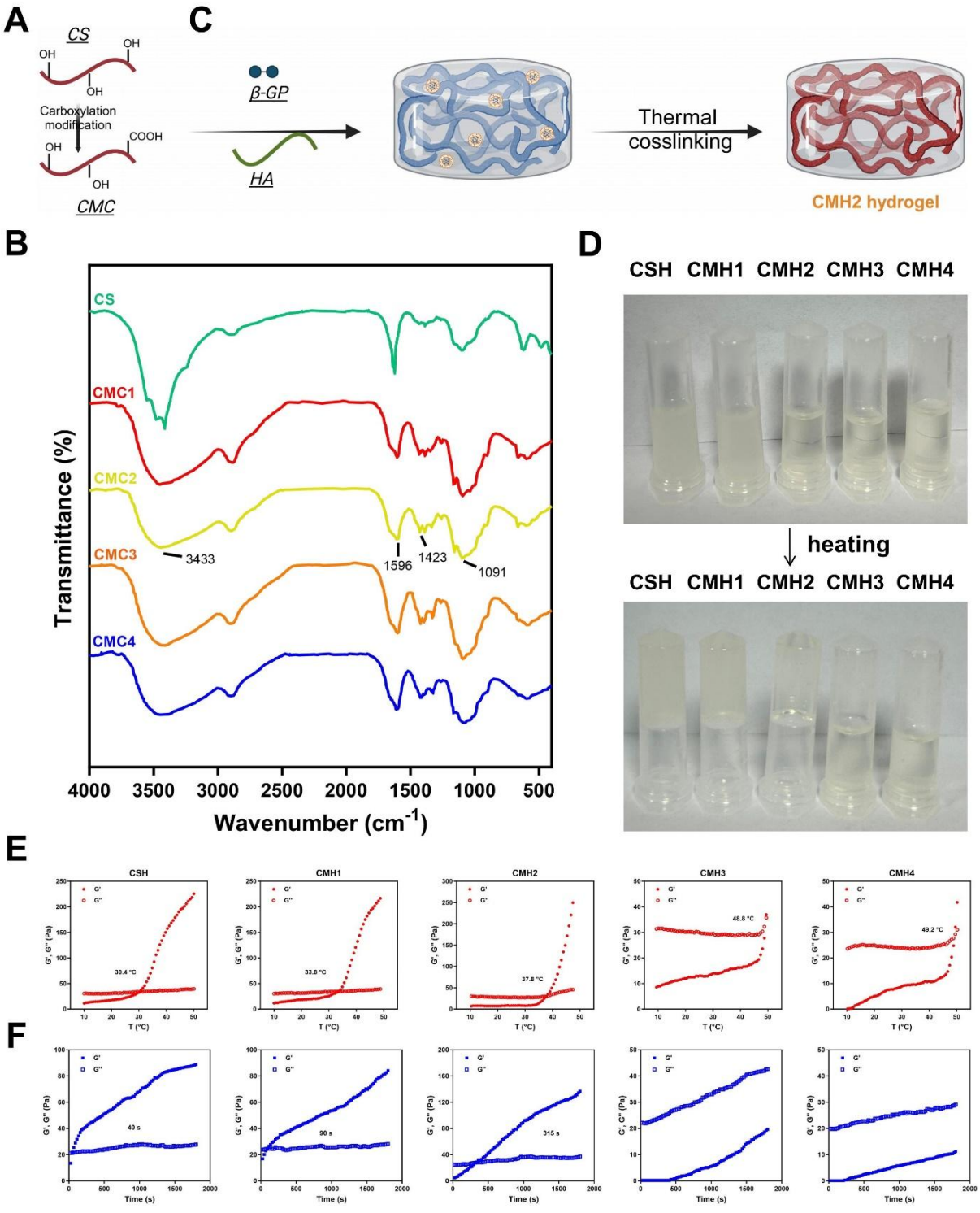

Figure S12. Carboxymethylation of CS and preparation and characterization of CMH2 thermosensitive hydrogel.

Note: (A) Schematic diagram of CMC synthesis via chloroacetic acid oxidation of CS; (B) FTIR spectra comparing structural differences between CS and CMC1-4; (C) Schematic illustration of CMH1-4 formation by crosslinking CMC1-4 with HA using β-GP; (D-E) Sol-gel transition assays

demonstrating temperature responsiveness of CMH1-4 hydrogels; (F) Rheological analysis of T_{gel} of CMH1-4 hydrogels.

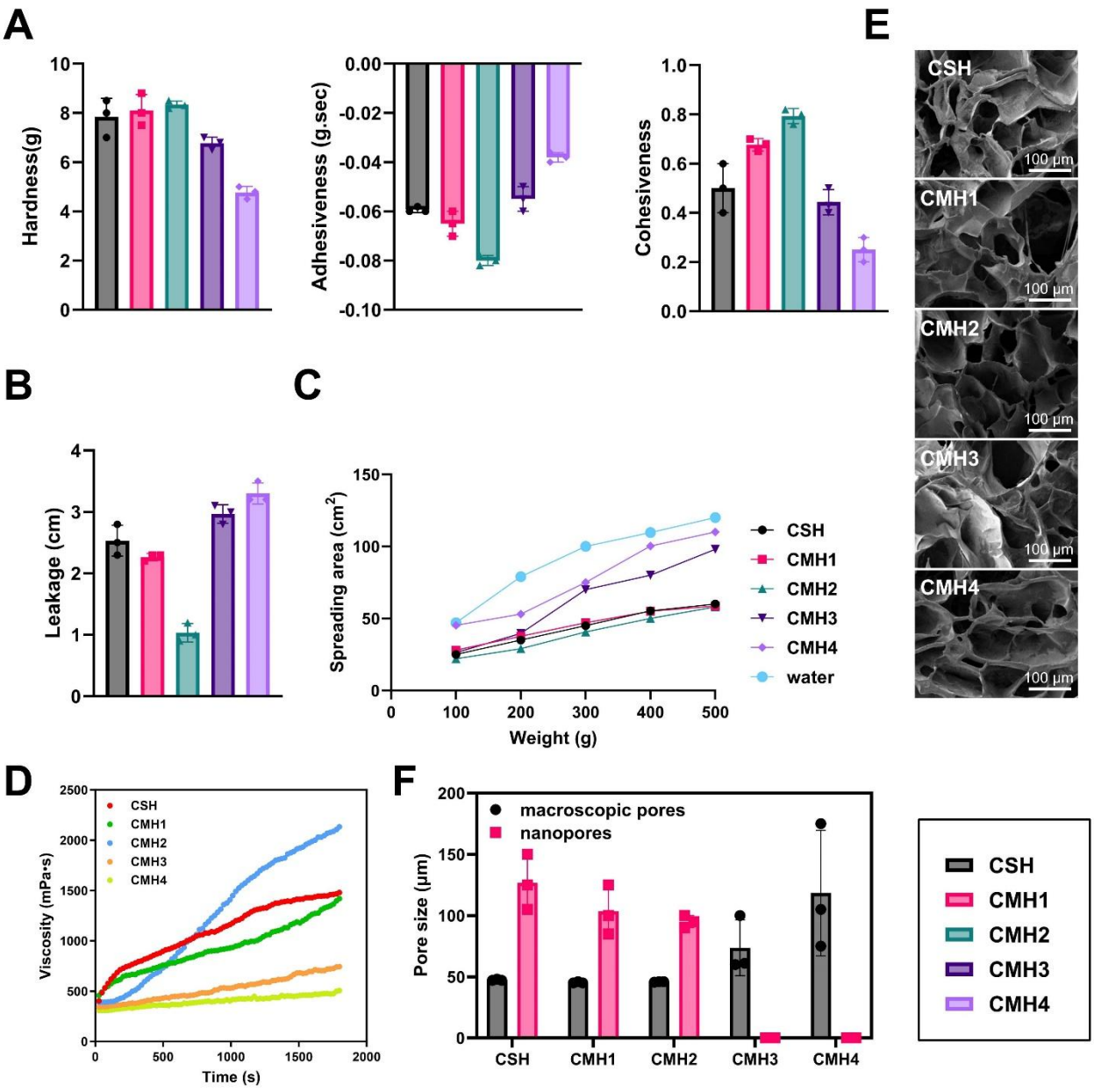

Figure S13. Skin conformability and microstructural characterization of CMH hydrogels.

Note: (A) Textural profile analysis of CMH1-4 hydrogels assessing hardness, adhesiveness, and cohesiveness; (B) Evaluation of skin adhesion using agar plates simulating skin surface; (C) Measurement of hydrogel spreadability under varying pressures; (D) Viscosity profile of CMH1-4 hydrogels during sol-gel transition at 37 °C; (E-F) SEM images showing the microstructure of CMH1-4 hydrogels, scale bar: 100 μm. Experiments were repeated three times.

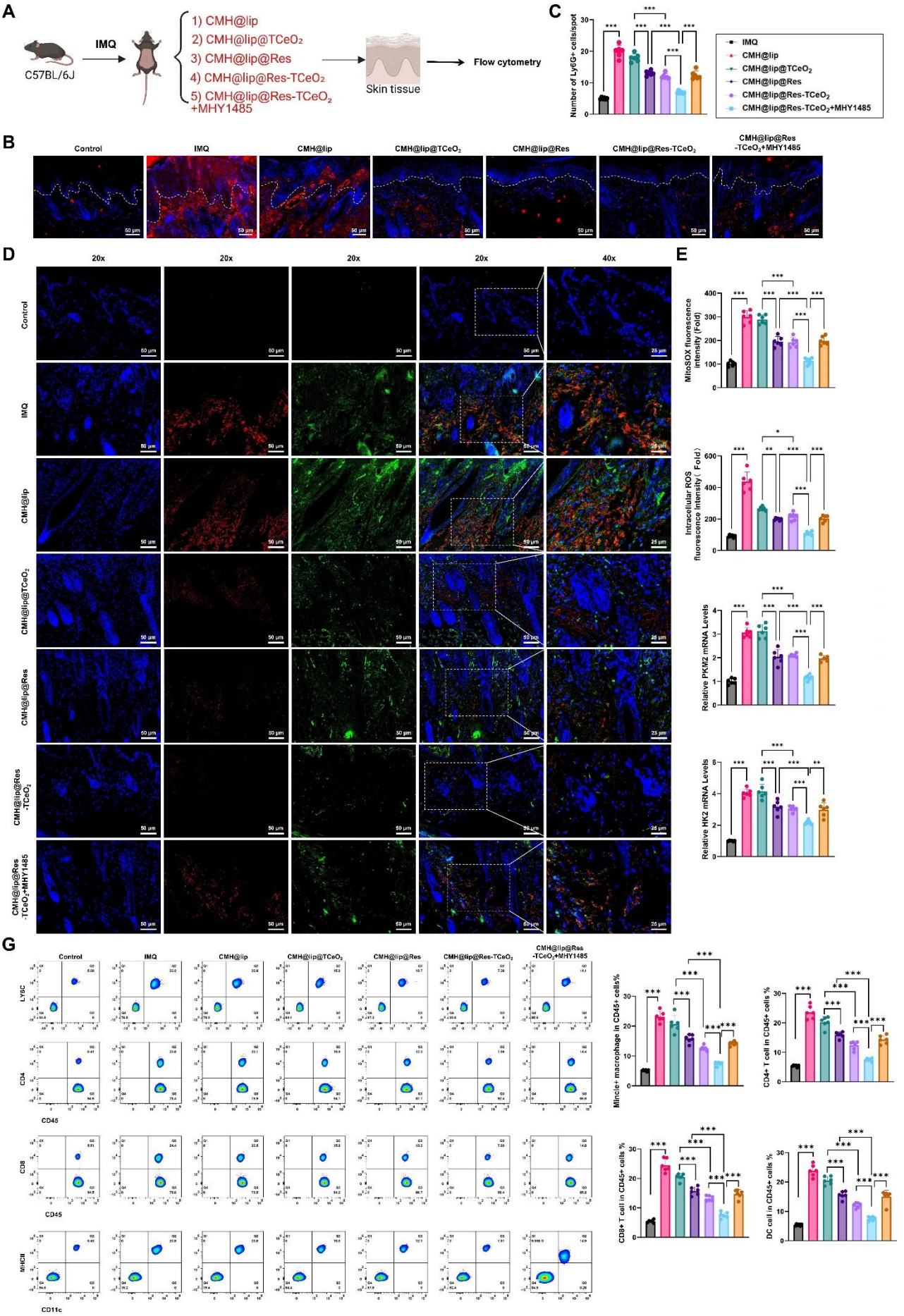
A
C57BL/6J
IMQ
1) CMH@lip
2) CMH@lip@TCeO2
3) CMH@lip@Res
4) CMH@lip@Res-TCeO2
5) CMH@lip@Res-TCeO2 +MHY1485
Skin tissue
Flow cytometry
C
Number of Ly6G+ cells/spot
IMQ
CMH@lip
CMH@lip@TCeO2
CMH@lip@Res
CMH@lip@Res-TCeO2
CMH@lip@Res-TCeO2+MHY1485
B
Control
IMQ
CMH@lip
CMH@lip@TCeO2
CMH@lip@Res
CMH@lip@Res-TCeO2
CMH@lip@Res -TCeO2+MHY1485
D
20x
20x
20x
20x
40x
Control
IMQ
CMH@lip
CMH@lip@TCeO2
CMH@lip@Res
CMH@lip@Res -TCeO2
CMH@lip@Res -TCeO2+MHY1485
E
MitoSOX fluorescence intensity (Fold)
Intracellular ROS fluorescence intensity (Fold)
Relative PKM2 mRNA Levels
Relative HK2 mRNA Levels
G
Control
IMQ
CMH@lip
CMH@lip@TCeO2
CMH@lip@Res
CMH@lip@Res-TCeO2
CMH@lip@Res -TCeO2+MHY1485
Ly6C
CD4
CD45
CD8
CD45
MHCII
CD11c
Mincle+ macrophage in CD45+ cells%
CD4+ T cell in CD45+ cells %
CD8+ T cell in CD45+ cells %
DC cell in CD45+ cells %

Figure S14. Effects of CMH@lip@Res-TCeO$_2$ on neutrophil infiltration, NETs formation, and infiltration of other immune cells in IMQ-induced skin tissues.

Note: (A) Schematic diagram illustrating the treatment strategy of CMH@lip@Res-TCeO$_2$; (B-C) IF staining of Ly6G and MPO to assess neutrophil infiltration in skin tissues, bar = 50 μm; (D) IF co-localization of Cit-H3 and extracellular DNA to evaluate NETs formation in skin tissues, bar = 25 μm; (E) CLSM analysis of total and mitochondrial ROS levels in neutrophils isolated from skin tissues; (F) RT-qPCR analysis of HK2 and PKM2 mRNA expression in skin-derived neutrophils; (G) Flow cytometry detection of activated macrophages, $CD4^+$ T cells, $CD8^+$ T cells, and DCs. n = 6 per group. Experiments were repeated three times. *$p < 0.05$, **$p < 0.01$, ***$p < 0.001$.

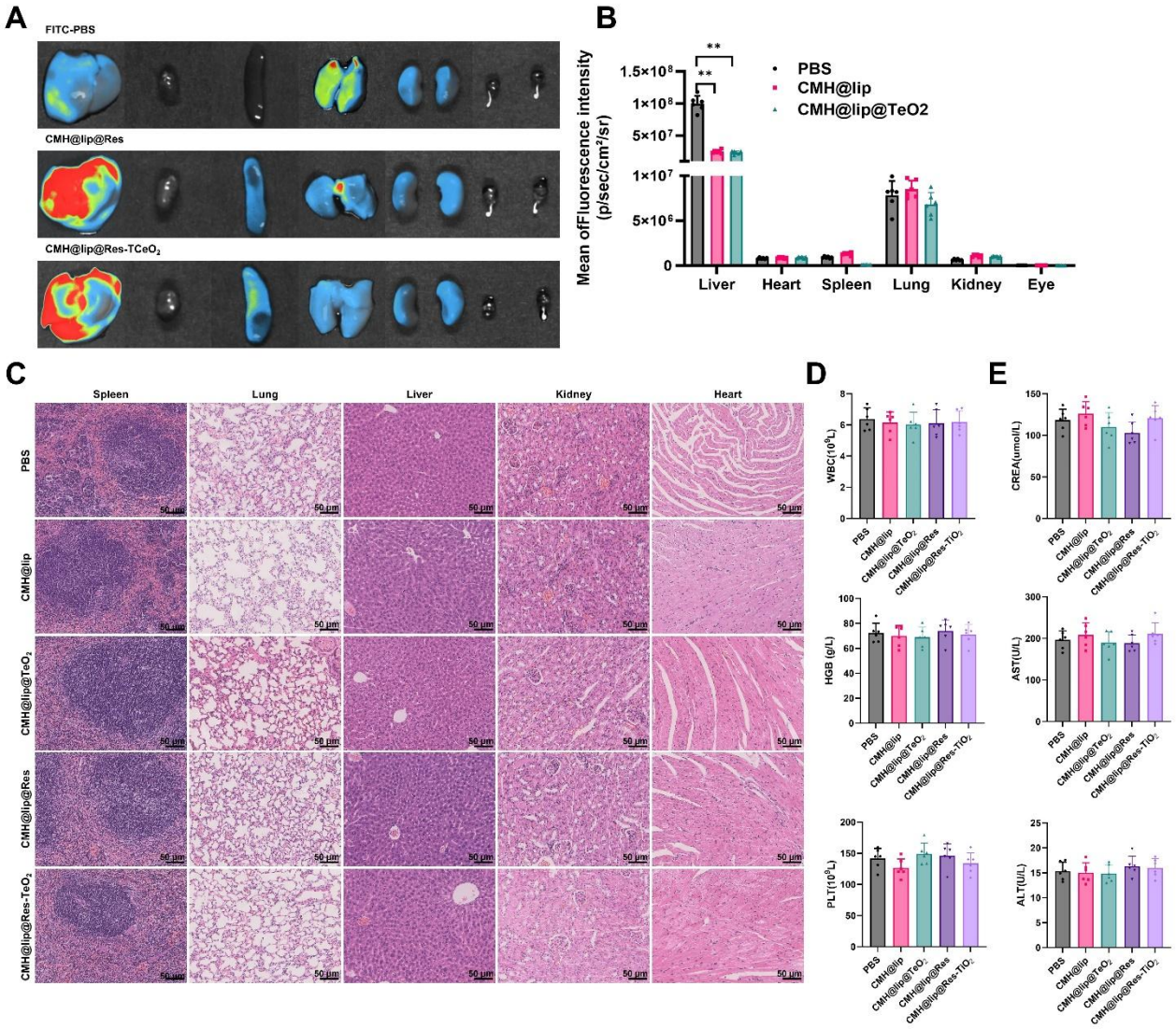

Figure S15. Systemic toxicity and biodistribution of CMH@lip@Res-TCeO$_2$.

Note: (A) Biodistribution in major organs at different time points; (B) Quantitative analysis of panel A data (mean ± S.D., n = 6); (C) H&E staining of major organs; (D) Routine hematological examination after treatment; (E) Serum biochemical analysis after treatment.

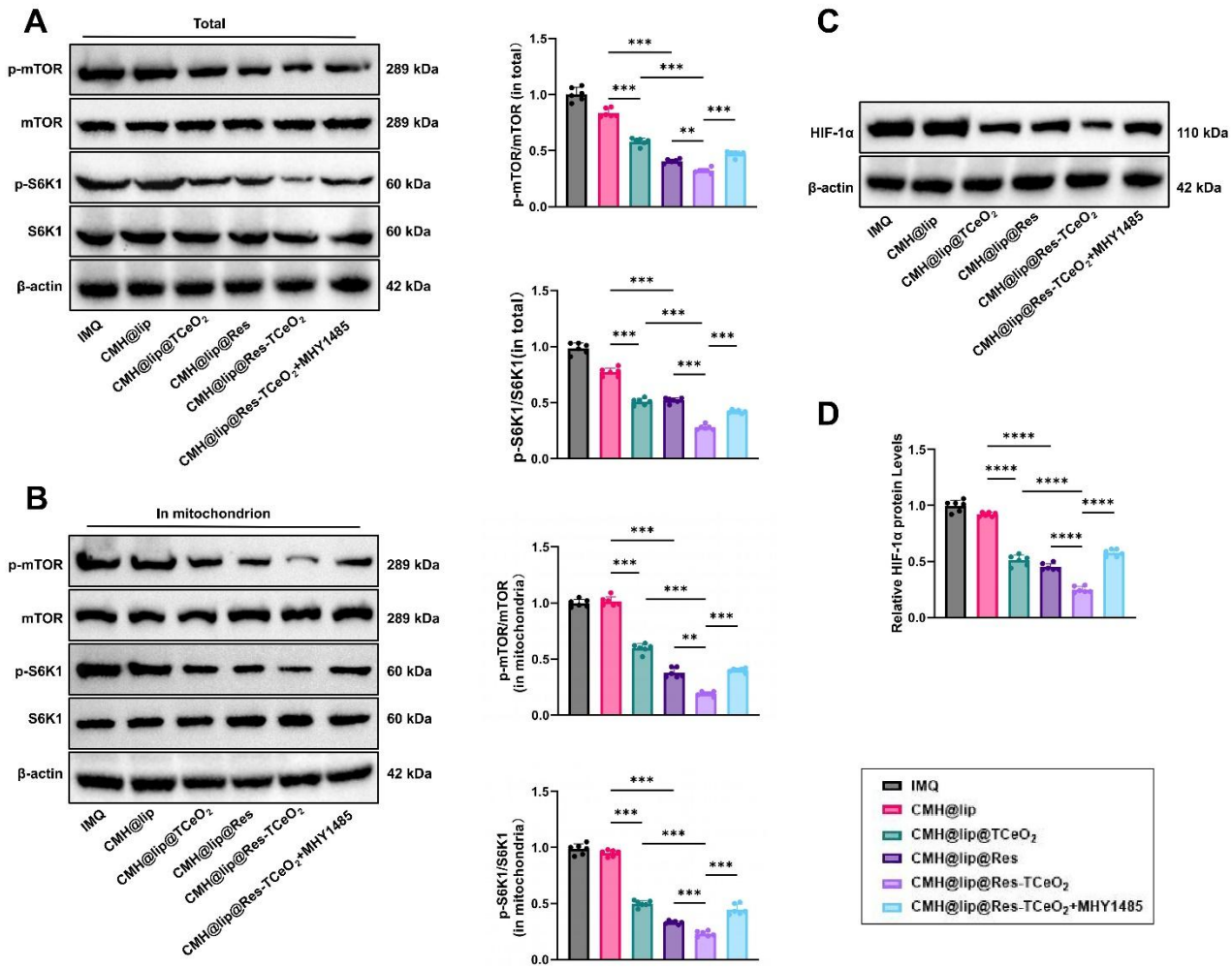

Figure S16. *In vivo* validation of the CMH@lip@Res-TCeO$_2$-mediated ROS/mTOR/HIF-1α axis.

Note: (A-B) Western blot analysis of total and mitochondrial protein levels of p-mTOR, mTOR, p-S6K1, and S6K1 in skin tissues; (C-D) Western blot analysis of HIF-1α protein expression in skin tissues. n = 6 per group. *$p < 0.05$, **$p < 0.01$, ***$p < 0.001$.